Sustainable Energy & Fuels

ROYAL SOCIETY OF CHEMISTRY

PAPER

View Article Online
View Journal | View Issue

Cite this: *Sustainable Energy Fuels*, 2025, **9**, 2769

Dopant-free hydrophobic fluorene-based hole transport materials: impact of methoxy-substituted triphenylamine and carbazole peripheral groups on the performance of perovskite solar cells†

Vighneshwar Ganesh Bhat, [a] Kavya S. Keremane, *[b] Subramanya K. S., [a] Archana S., [a] Akash Hegde, [a] Ivy M. Asuo, [b] Bed Poudel [b] and Udaya Kumar Dalimba *[a]

Hole-transporting materials (HTMs) are crucial for charge separation in perovskite solar cells (PVSCs). Besides possessing suitable HOMO/LUMO energies, HTMs should ideally be hydrophobic to protect the perovskites from atmospheric moisture to enhance device stability. We designed two fluorene-core D–π–D-type organic HTMs (**V1** and **V2**), consisting of either 4,4′-methoxy triphenylamine (**V1**) or *N*-phenyl-3,6-methoxy carbazole (**V2**) as the peripheral donor moiety. Optoelectronic characterization and density functional theory calculations confirmed the intramolecular charge transfer within these new HTMs. UPS and REELS analyses revealed favorable HOMO–LUMO energy level alignment of **V1** and **V2** with the work functions of $MAPbI_3$ and gold electrode for effective charge extraction. TRPL and transient absorption studies commendably explained better quenching of perovskite's luminescence by **V1** over **V2**, suggesting a better interfacial contact of **V1** with the perovskite layer. Accordingly, the PVSCs with **V1** and **V2** as HTMs in an architecture ITO/SnO_2/$MAPbI_3$/HTM(**V1** or **V2**)/Au demonstrated power conversion efficiency (PCE) of 14.05% and 12.73% respectively. Also, the device with **V1** retains 75% of its initial efficiency for more than 480 hours. The contact angle measurements revealed the strong hydrophobicity of both alkylated fluorene molecules (**V1** and **V2**), and impedance spectroscopy measurements further revealed higher R_{rec} values for these HTMs, indicating improved charge transport and reduced recombination losses. These findings demonstrate the potential of the newly developed hydrophobic fluorene-based HTMs for achieving long-lasting performance in PVSCs.

Received 25th January 2025
Accepted 10th April 2025

DOI: 10.1039/d5se00120j

rsc.li/sustainable-energy

1. Introduction

Charge-transporting materials (CTMs) are crucial components of perovskite solar cells (PVSCs), which assist in the conversion of photo-generated excitons into respective charge carriers (*i.e.* holes and electrons). Hole-transporting material (HTM) plays a key role in the device performance by effectively extracting kinetically slow-moving holes and blocking the electron transfer from the perovskite layer to the counter electrode.[1] Additionally, they can also protect the perovskite layer from the surrounding degrading environmental factors like moisture and oxygen. Till today, many inorganic HTMs like NiO_x, CuSCN, VO_x, MoO_x, *etc.*, have been utilized in PVSCs, which resulted in power conversion efficiency (PCE) of up to 21%. However, their relatively low water and oxygen resistance results in devices with poor long-term stability.[2–4] Organic HTMs, on the other hand, possess many superior properties such as good hydrophobicity, band gap tunability, good film-forming ability, low cost, and compatibility with simpler fabrication methods at lower temperatures.[5–7] The compounds Spiro-OMeTAD and PTAA are the most well-studied and efficient organic HTMs in the last decade (PCE up to 24%).[1] However, these materials require a foreign substance called a 'dopant' to improve their electrical properties. Frequently used dopants are 4-*tert*-butyl pyridine (4-*t*BP) and lithium bis(trifluoromethanesulfonyl)imide (Li-TFSI), which are ionic in nature and hence make the HTL relatively hydrophilic.[8,9] Also, upon using 4-*t*BP as a dopant for HTMs, the pyridination of oxidized HTMs under thermal stress lowers their conductivity.[10,11] Similarly, diffusion of halide ion (especially I_3^-) from perovskite to HTM reduces the oxidized HTM to a neutral state, causing loss of their hole mobility.[12] All these factors lead to the deterioration of the perovskite layer. Henceforth, there is a demand for dopant-free alternative small-molecular hydrophobic HTMs that are

[a]*Organic and Materials Chemistry Laboratory, Department of Chemistry, National Institute of Technology Karnataka, Surathkal, 575025, Mangalore, Karnataka, India. E-mail: udayakumar@nitk.edu.in*

[b]*Department of Materials Science and Engineering, The Pennsylvania State University, University Park, PA, USA. E-mail: kxk5889@psu.edu*

† Electronic supplementary information (ESI) available. See DOI: https://doi.org/10.1039/d5se00120j

chemically compatible with the perovskite, to control PVSCs' degradation and improve the device stability. As these perovskite materials are ionic in nature, they are less stable in the presence of moisture, oxygen, light and elevated temperature during both the fabrication and operational phases of the devices.[13] Hence, it is necessary to use stable surrounding materials such as HTMs, that are less reactive towards atmospheric conditions in order to improve the device stability.

In this context, there is a growing need to develop hydrophobic HTMs for PVSCs to enhance stability while ensuring simpler synthesis methods that can lower production costs.[14,15] Different kinds of small molecule HTMs based on carbazole, fluorene, thiophene, phenazine and triphenylamine (TPA) cores have been reported in the last few years.[1,16] Among these materials, HTMs designed with fluorene cores possess good charge mobility, excellent solubility in conventional organic solvents, good film formation properties, and robust chemical stability, making them strong candidates for advancing PVSC technology.[17,18] Fluorene-based HTMs present a compelling alternative to traditional materials like Spiro-OMeTAD and PTAA. Their attractiveness lies in several advantageous properties: they are straightforward to synthesize, easily functionalized through their active sites, and possess distinctively deep HOMO and elevated LUMO energy levels, making them efficient electron blockers.[19,20] Additionally, fluorene is a weak electron donor and introducing alkyl chains at the C9 of fluorene enhances its hydrophobic character, film-formation ability, and improved solubility. The rigid and planar structure of fluorene contributes to the thermal stability of HTMs, which is essential for ensuring the long-term performance of PVSCs under operational conditions. Therefore, fluorene serves as an excellent core moiety for designing HTMs for PVSCs.[17,21] The electronic properties of HTMs can be finely tuned by incorporating thiophene π-bridges, which facilitate better alignment of the HTM's energy levels with the perovskite layer, thereby enhancing hole extraction efficiency.[14,22] The inclusion of π-bridges in the molecular design extends the π-conjugation length, improving hole mobility and reducing charge recombination losses.

Small molecule HTMs with a D–π–D architecture typically exhibit strong intramolecular charge transfer characteristics, influencing their bandgap and absorption properties while potentially enhancing intermolecular packing in thin films and improving charge carrier mobility.[23,24] However, these HTMs often face challenges such as suboptimal performance, limited stability, and reliance on high dopant concentrations when applied in PSCs. Therefore, it is essential to systematically investigate the state-of-the-art heterocyclic peripheral donor units in dopant-free HTMs and their impact on structural stability, hydrophobicity, and overall device performance. The 4,4′-methoxy triphenylamine is the widely utilized peripheral moiety for designing many HTMs[25,26] due to its effective electron-donating ability, good hole-transporting and film-forming capabilities. One of its main advantages is the ease with which the central nitrogen atom can be oxidized, allowing for efficient hole transfer through a radical cationic state during device operation.[27] To catalyze the formation of such radical ions, we designed another peripheral moiety with *N*-phenyl-3,6-methoxy carbazole, where two of the phenyl groups of the triphenylamine are interconnected, making it a complete rigid aromatic system.[28] The carbazole moiety is recognized as an electron-rich donor exhibiting strong electron-donating capabilities, effective hole transport, and favorable film formation properties, making it a prominent component in designing hole transport materials.[29] To study the effect of such rigidity in a donor moiety of a HTM, we have developed two dopant-free fluorene-based HTMs, **V1** and **V2** (Scheme 1), containing 4,4′-methoxy triphenylamine and *N*-phenyl-3,6-methoxy carbazole as peripheral donor groups, respectively. The molecules, **V1** and **V2**, adopt a D–π–D architecture, with a symmetrically alkylated fluorene moiety as the core, which serves as both a weak donor and a π-linker, leveraging the benefits of easily tunable energy levels and extended π-conjugation length to enhance charge transport properties. A thiophene moiety in these molecules acts as a π-linker between the peripheral donor groups and the core. The octyl groups placed at the C9 of the fluorene moiety are expected to bring the required hydrophobicity to the molecule. This design approach also improves molecular packing, which enhances charge transport properties.

To evaluate the impact of the developed HTMs on PVSCs, a conventional n–i–p model (negative–intrinsic–positive) was utilized for fabrication with an architecture ITO/ETM/$MAPbI_3$/HTL/Au. Here 'n' and 'p' represent the electron transporting material (ETM) and HTM respectively, and 'i' represents the perovskite absorber layer.[30] Many inorganic ETMs like TiO_2, SnO_2, CeO_x, WO_x, In_2S_3, *etc.* have been studied for PVSCs applications.[31] Among these materials, TiO_2 is a widely studied ETM in the PVSCs. However, it has a dark face of low electron mobility, high UV photocatalytic activity towards perovskite degradation, and high crystallization temperature (400–500 °C) during deposition.[32,33] On the other hand, SnO_2 can take over an advantage with a superiority in all these factors and being processable at temperatures below 200 °C (which is very useful for flexible electronics). Likewise, ZnO fails to match SnO_2's performance in all these criteria.[34–36] In this study, PVSCs with **V1** and **V2** as HTM showed efficiency of 14.05% and 12.73% respectively. The 4,4′-methoxy triphenylamine (**V1**) donor moiety performed better than the *N*-phenyl-3,6-methoxy carbazole (**V2**) group.

2. Materials and methods

2.1. Characterization methods

The structures of all synthesized intermediates and final compounds were elucidated using ^{1}H NMR (400 MHz, Bruker Avance), ^{13}C NMR (100 MHz, Bruker Avance), HR-MS (Xevo G2-XS QTof, Waters, USA), and MALDI-TOF Mass (Autoflex Speed, Bruker) spectral techniques. ^{1}H NMR spectra were recorded in $CDCl_3$ with *tetra*-methyl silane (TMS) as an internal standard. ^{13}C NMR spectra were recorded in $CDCl_3$ (without TMS, and solvent peak at δ_{ppm} 77.65 as the reference peak). The chemical shifts are expressed in terms of δ_{ppm} and peak multiplicities are reported as 's' for a singlet, 'd' for a doublet, 't' for a triplet, 'dd' for a doublet of doublets, and 'm' for a multiplet. '*J*' represents the coupling constant of a multiplet. The UV-visible and fluorescence spectral

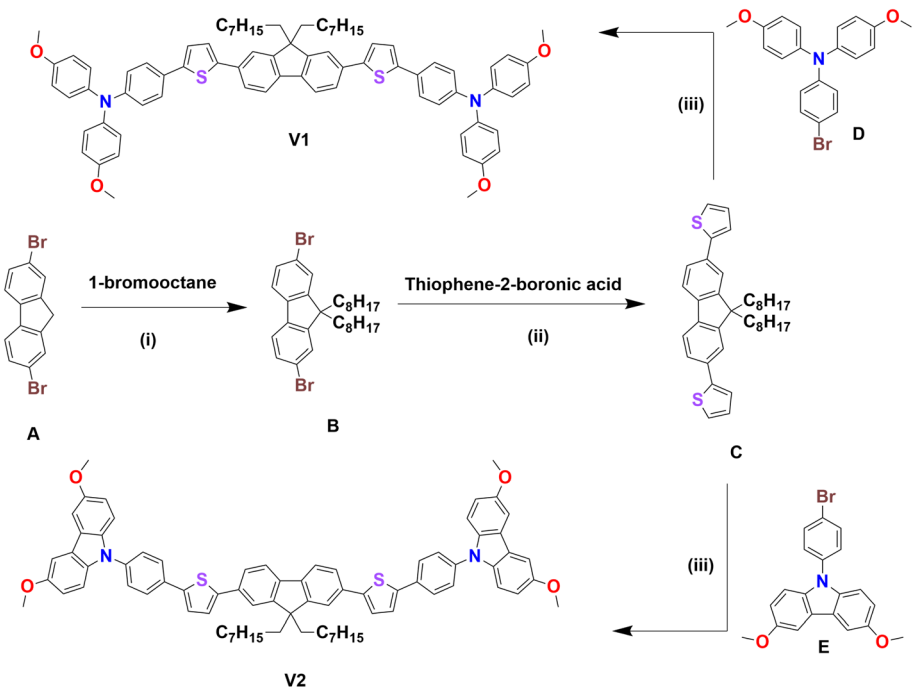

Scheme 1 (i) DMSO, NaOH, KI, TBAB, 90 °C, hours. (ii) $Pd(PPh_3)_4$, K_2CO_3, toluene : ethanol (3 : 1), argon, reflux, 4 hours. (iii) $Pd(OAc)_2$, t-Bu_3-P·HBF_4, PivOH, K_2CO_3, DMA, argon, 120 °C, 26 hours.

analysis (for liquid state) for the synthesized compounds were carried out using an Analytik Jena SPECORD S 600 spectrometer and a Jasco FP 6200 spectrophotometer, respectively. Steady-state photoluminescence (PL) and time-resolved photoluminescence (TRPL) spectra were collected by an FLS1000 fluorescence spectrometer (Edinburgh Instrument) at room temperature. For time-resolved PL measurement, a 506 nm picosecond pulsed diode laser was used as an excitation source. Signals were collected by a time-correlated single-photon counting (TCSPC) detector. UV-vis absorption spectroscopy was performed by a UH4150 (Hitachi) spectrometer at room temperature. Thermogravimetric analysis (TGA) was carried out using a TGA 4000 (PerkinElmer) with a heating rate of 5 °C min^{-1} under a nitrogen environment. HOMO and LUMO energy levels of the compounds were determined using their thin films deposited on FTO through ultraviolet photoelectron spectroscopy (UPS) and reflection electron energy loss spectroscopy (REELS) methods by using NEXSA Surface Analysis (Thermo Scientific). For UPS analysis HeI (21.2 eV) is used as a light source, and a biasing voltage of −5 V was applied. For REELS analysis 250 eV beam energy was utilized. Density functional theory (DFT) studies for the designed compounds were performed using Schrodinger's Material Science 3.9 package with the B3LYP functional theory and 6-311G** basis set for structural optimization. The formation of the perovskite state during the fabrication is analyzed using X-ray diffraction (X-RD) with a Malvern Panalytical Empyrean IV, PIXcel 3D, and 1Der detector. To explore the morphology of the perovskite thin film and the microstructural evolution of the device architecture, we employed surface and cross-sectional field-emission scanning electron microscopy (FE-SEM) respectively with a Zeiss Merlin field-emission scanning electron microscope (FE-SEM). The transient absorption studies, including transient photocurrent (TPC) and transient photovoltage (TPV), as well as electrochemical impedance spectroscopy (EIS), were conducted using the Fluxim AG Paios system, which is equipped with a white LED as the light source. The photovoltaic performance of the solar cells was evaluated by the *J–V* characteristics of the devices measured under a Newport solar simulator, which produced simulated AM 1.5G solar irradiation generated by a Xenon lamp (Oriel Sol 2A ABA). The solar simulator was calibrated by a standard reference silicon cell covered with KG5 filter glass. *J–V* characteristics were measured using a Keithley 2400 source meter with a scan step of 0.02 V and a scan rate of 0.1 V s^{-1} with an active area of 0.086 cm^2. The IPCE was obtained on the QTest Station 2000ADI system (Crowntech. Inc., USA). The unencapsulated PVSCs were stored in an ambient atmosphere at room temperature (24–28 °C) with relative humidity of 60% for stability analysis and were analyzed at different time intervals. Maximum power point (MPP) tracking stability tests were done under continuous one-sun illumination (AM 1.5G, 100 mW cm^{-2}) at room temperature. Contact angle measurements were performed to determine the hydrophobicity of the compounds (as thin films deposited on glass substrates) using an automated Goniometer/Tensiometer with Environmental Chamber Support (ramé-hart Model 295 F4 series), and images were captured within 5 s of water droplets being placed on the surface.

2.2. Synthesis

Scheme 1 and Fig. S1† depicts the synthetic pathway for the new molecules **V1** and **V2**. The synthetic procedure and spectral characterization details of **V1** and **V2** are described here, whereas the same for the intermediates are given in the ESI.†

2.2.1. Synthesis of hole-transporting materials (V1 and V2). Intermediate **C** (100 mg, 0.180 mmol) and intermediate **D** (or **E**) (0.432 mmol) were taken in a clean and dry reaction tube along with K_2CO_3 (1.08 mmol). Subsequently, pivalic acid (0.216 mmol), *t*-$Bu_3P\cdot HBF_4$ (0.072 mmol), and *N*,*N*′-dimethylacetamide (0.6 mL, 0.3 M) were added to the reaction tube. Finally, $Pd(OAc)_2$ (0.018 mmol) was added as a catalyst and the reaction mixture was heated to 120 °C for 26 hours under argon. After the completion of the reaction, the crude product was extracted with dichloromethane (DCM) against water. The organic layer was dried using anhyd. Na_2SO_4, and concentrated. The crude solid was purified using column chromatography (silica gel: mesh size of 100–200) with pet ether/DCM (7 : 3) mixture as the eluting system.

4,4′-((9,9-Dioctyl-9*H*-fluorene-2,7-diyl)bis(thiophene-5,2-diyl))bis(*N*,*N*-bis(4-methoxy phenyl)aniline) (**V1**): brownish yellow solid; yield: 60%; ^{1}H NMR ($CDCl_3$, 400 MHz): δ_H 7.66 (2H, d, J = 7.9 Hz, Ar–H), 7.59 (2H, dd, J = 1.6, 7.9 Hz, Ar–H), 7.55 (2H, d, J = 1.2 Hz, Ar–H), 7.45 (4H, d, J = 8.8 Hz, Ar–H), 7.32 (2H, d, J = 3.8 Hz, Ar–H), 7.18 (2H, d, J = 3.7 Hz, Ar–H), 7.09 (8H, d, J = 8.9 Hz, Ar–H), 6.94 (4H, d, J = 8.6 Hz, Ar–H), 6.85 (8H, dd, J = 2.2, 6.8 Hz, Ar–H), 3.81 (12H, s, O–CH_3), 2.06–1.98 (4H, m, CH_2), 1.20–1.03 (24H, m, CH_2), 0.78 (6H, t, J = 7.0 Hz, CH_3); ^{13}C NMR ($CDCl_3$, 100 MHz): δ_C 156.01, 151.70, 148.24, 143.66, 142.94, 140.68, 140.07, 133.30, 126.68, 126.26, 124.46, 123.76, 122.63, 120.55, 120.02, 119.62, 114.76, 55.52, 55.26, 40.44, 31.80, 30.01, 29.71, 29.23, 23.76, 22.60, 14.07; MALDI-TOF MS analysis (*m*/*z*): mol. formula: $C_{77}H_{80}N_2O_4S_2$, calculated: 1160.556, found: 1161.522 $[M + H]^+$.

9,9′-(((9,9-Dioctyl-9*H*-fluorene-2,7-diyl)bis(thiophene-5,2-diyl))bis(4,1-phenylene)) bis(3,6-dimethoxy-9*H*-carbazole) (**V2**): yellow solid, yield: 62%; ^{1}H NMR ($CDCl_3$, 400 MHz): δ_H 7.86 (4H, d, J = 8.4 Hz, Ar–H), 7.74 (2H, d, J = 7.9 Hz, Ar–H), 7.67 (2H, d, J = 8.0 Hz, Ar–H), 7.63 (2H, s, Ar–H), 7.60 (2H, s, Ar–H), 7.57 (6H, d, J = 2.5 Hz, Ar–H), 7.45–7.38 (8H, m, Ar–H), 7.07 (4H, dd, J = 2.5, 8.9 Hz, Ar–H), 3.97 (12H, s, O–CH_3), 2.11–2.03 (4H, m, CH_2), 1.22–1.06 (24H, m, CH_2), 0.80 (6H, t, J = 7.0 Hz, CH_3); ^{13}C NMR ($CDCl_3$, 100 MHz) δ_C 154.13, 151.84, 144.76, 142.35, 140.38, 137.31, 136.12, 133.10, 132.93, 126.95, 126.82, 124.73, 124.43, 124.02, 123.75, 120.23, 119.83, 115.24, 110.77, 102.95, 56.12, 55.35, 40.42, 31.81, 29.99, 29.70, 29.66, 29.23, 29.19, 23.78, 22.61, 14.08; MALDI-TOF analysis (*m*/*z*): mol. formula: $C_{77}H_{76}N_2O_4S_2$, calculated: 1156.525, found: 1157.728 $[M + H]^+$.

2.3. Fabrication of perovskite solar cells

2.3.1. Materials used for fabrication. The substrate used for PVSCs fabrication was indium-doped tin oxide-coated glass (ITO; sheet resistance 12–20 Ω per sq.) sourced from Colorado concept coating LLC. Lead iodide (PbI_2, 99.9985% metals basis) and the SnO_2 solution (tin(IV) oxide, 15 wt% in H_2O colloidal dispersion) were purchased from Alfa Aesar. Methylammonium iodide (CH_3NH_3I (MAI)) was purchased from Greatcell Solar Materials. 4-*t*BP (98%), Li-TSFI (99.95%), spiro-OmeTAD (99%), methylamine solution (MA, 33 wt% in absolute ethanol), and anhydrous acetonitrile (AcCN, 99.8%) were purchased from Sigma-Aldrich. Gold (Au, 99.99%) was purchased from Angstrom Engineering Inc. All materials were used as acquired without further processing.

2.3.2. Fabrication of PVSCs. The solar cell device employs a typical n–i–p configuration with an architecture ITO/SnO_2/$MAPbI_3$/HTL/Au. ITO glass was successively cleaned with acetone, distilled water, and ethanol for 30 minutes. After drying, the ITO glasses were treated with UV-ozone for 30 min. The SnO_2 thin films were deposited onto ITO by spin-coating of solution at 3000 rpm for 35 s, following which the as-deposited film was annealed at 150 °C for 30 min. Next, the substrate was transferred into a glovebox, the perovskite photoactive layer was deposited by spin-coating the prepared precursor solution at 4000 rpm for 35 s without annealing. During the perovskite crystallization process, the bi-layer characteristics (top nanocrystalline capping layer/bottom typical large perovskite grains) are self-assembled. All the different HTMs were dissolved in chlorobenzene with a concentration of 20 mM without using any dopants. All the HTL layers were deposited on the perovskite layer by spin-coating the solution at 4000 rpm for 35 s. Finally, an 80 nm gold layer was deposited on HTL by thermal evaporation as the electrode, with the active device area fixed to 0.086 cm^2 using a shadow mask.

2.3.3. Preparation of $MAPbI_3$ stock solution. 159 mg MAI and 461 mg PbI_2 (1 : 1 ratio) powders are taken in a vial and dissolved in freshly prepared 0.5 mL methylamine solution (MA, 33 wt% in absolute ethanol). The vial was directly sonicated for 1 hour until the solution became completely clear. After obtaining a clear solution from the sonication, 500 μL AcCN solvent was added to dilute the system. After a quick sonication for 5 min, the $MAPbI_3$ perovskite precursor solution was directly utilized. All solutions were filtered before solution casting.[37]

2.3.4. Preparation of Spiro-OMeTAD stock solution. Spiro-OMeTAD is used as a reference HTM for validating results during the fabrication of PVSCs. A stock solution was prepared by dissolving 72 mg of Spiro-OMeTAD in 1 mL of chlorobenzene with 26 μL of 4-*t*BP and 13 μL of 520 mg per mL Li-TSFI in acetonitrile. The Spiro-OMeTAD layer was then deposited using the same process as the synthesized HTMs.

3. Results and discussion

3.1. Synthesis of fluorene-based hole-transporting materials

The brief synthetic pathway for the newly designed HTMs **V1** and **V2** is shown in Scheme 1. Initially, the alkylation of 2,7-dibromo fluorene (**A**) was carried out using TBAB as a phase transfer catalyst (PTC) and a catalytic amount of KI as an accelerator to yield intermediate (**B**) which was then subjected to the Suzuki coupling reaction with thiophene-2-boronic acid to get compound (**C**) with a yield of 88%. The end group precursors 4-bromo-*N*,*N*-bis(4-methoxyphenyl)aniline (**D**) and dimethoxy-*N*-(bromophenyl) carbazole (**E**) were synthesized through Cu(I) assisted N–C coupling reactions (*i.e.* modern Ullmann coupling). The target molecules (**V1** and **V2**) were synthesized through a C–H activated coupling reaction between intermediate (**C**) and intermediate (**D**) [or (**E**)]; using $Pd(OAc)_2$ as a catalyst, (*t*-$Bu)_3P\cdot HBF_4$ as a ligand and pivalic acid as an

activator. All the intermediates and final compounds were characterized by NMR spectroscopy and mass spectrometry (ESI†).

3.2. Opto-electronic and thermal studies of the new HTMs

To investigate the optical behavior of the compounds **V1** and **V2**, their UV-vis and photoluminescence spectra were recorded in different organic solvents of varying polarity at a concentration of 6.67 μM. The resulting spectra are presented in Fig. 1(A) and Fig. 1(B), and the related absorption and emission parameters are summarized in Tables 1 and S1.† According to these solvatochromic absorption studies, the λ_{max} of the intramolecular charge transfer (ICT) band for compound **V1** shifts from 416 nm to 430 nm, and the same trend was observed for compound **V2** as well, where the λ_{max} shifts from 398 nm to 406 nm, depending upon the nature of the solvent. The ICT occurs from the donor groups (triphenylamine/*N*-phenyl carbazole) to the core moiety (fluorene) due to the extended conjugation in these molecules. In the acetonitrile solution, the λ_{max} for **V1** and **V2** is 416 nm ($\varepsilon = 76.64 \times 10^3$ M^{-1} cm^{-1}) and 398 nm ($\varepsilon = 126.91 \times 10^3$ M^{-1} cm^{-1}) respectively. The higher λ_{max} of **V1** compared to **V2** signifies that **V1** has better π-conjugation than **V2**. This is attributed to the triphenylamine moiety in **V1** being a more effective π-donor than the *N*-phenyl carbazole group in **V2**. In the thin-film state, the compounds **V1** and **V2** have shown λ_{max} of 432 nm and 413 nm respectively. Notably, these λ_{max} values are relatively higher than their corresponding solution state values, as shown in Fig. 1(C), due to the π-stacking effect in the solid state.

From the emission behavior, it is noticed that molecule **V1** has longer emission λ_{max} than **V2**. The emission λ_{max} for **V1** varies in the range of 477–508 nm, whereas **V2** showed λ_{max} in the range of 449–484 nm, depending on the nature of the solvent (Fig. 1(A) and (B)). In acetonitrile solution, compounds **V1** and **V2** showed λ_{max} of 502 nm and 476 nm, respectively. Notably, **V2** exhibits two intense bands (Fig. 1(B)), indicating the presence of two distinct relaxation pathways for the molecule. The polarity of the solvent remarkably influences the intensities of these bands. In a thin-film state, the emission λ_{max} for compounds **V1** and **V2** is 541 nm and 505 nm respectively, and both compounds resulted in two intense bands, signifying two distinctive de-excitation mechanisms. The Stokes shift (λ_{shift}) in acetonitrile solution for **V1** and **V2** is the largest *i.e.*, 86 nm and 78 nm, respectively, and the respective values in the film state are found to be 109 nm and 98 nm (from Fig. 1(C)). The optical

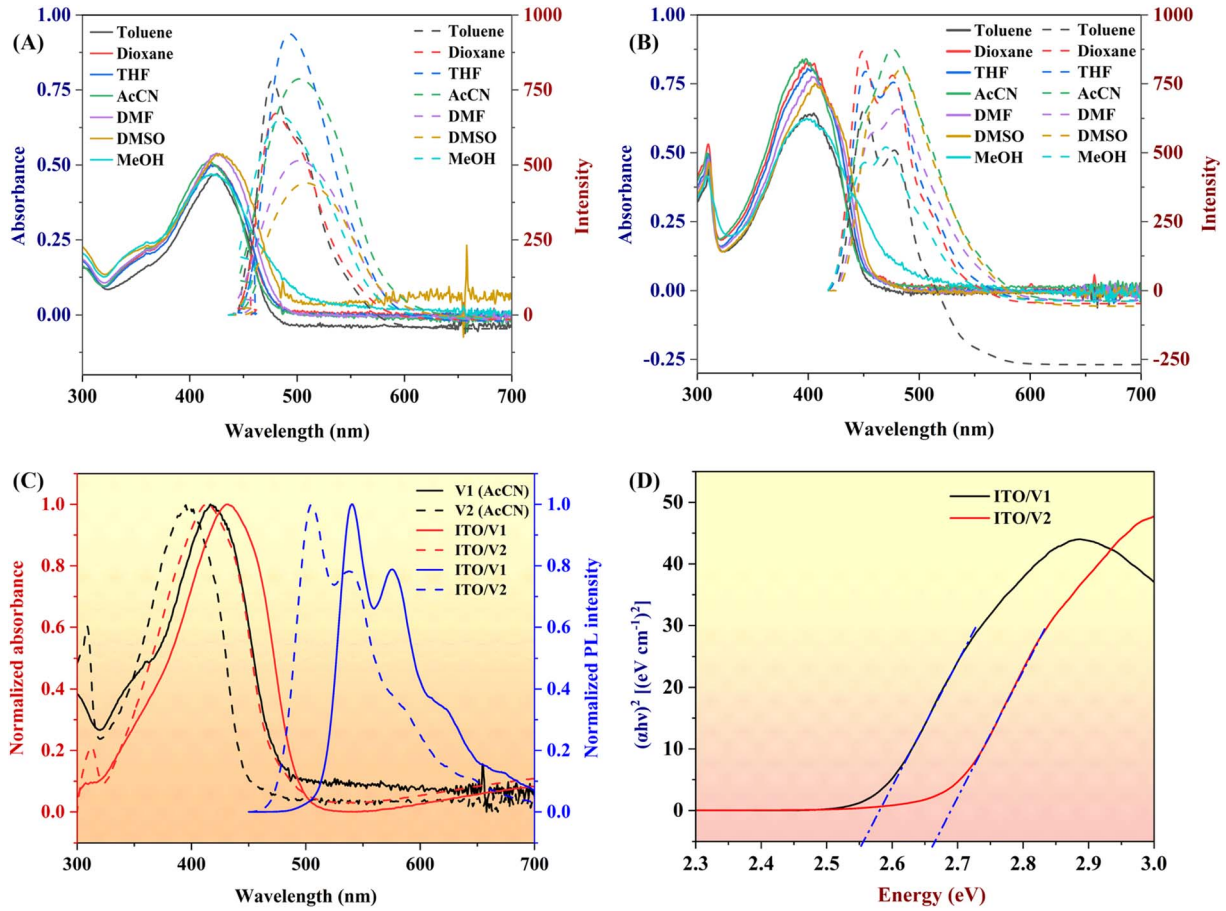

Fig. 1 (A) Solvatochromic absorption (solid line) and emission (dash line) spectra of compounds **V1**. (B) Solvatochromic absorption (solid line) and emission (dash line) spectra of compound **V2**. (C) Normalized absorption spectra of HTMs in liquid states (black lines), in thin-film state (red lines), and normalized emission (blue line) spectra of HTMs in the thin-film state. (D) Optical band gap of the compounds **V1** and **V2** from Tauc plot.

Table 1 Absorption and emission parameters, electronic band structure and thermal properties of compounds **V1** and **V2**[a]

HTM	Solution state[b]		Thin film state[c]		$\Delta\lambda^{Sol}/\Delta\lambda^{film}$ (nm)	$E_g^{soln}/E_g^{film}/E_g^{REELS}$ (eV)	E_{HOMO} (eV)	E_{LUMO} (eV)	T_d (°C)
	λ_{max}^{abs} (nm)	λ_{max}^{em} (nm)	λ_{max}^{abs} (nm)	λ_{max}^{em} (nm)					
V1	416	502	432	541	86/109	2.71/2.55/2.49	−5.14	−2.65	257
V2	398	476	413	505	78/98	2.85/2.66/2.52	−5.44	−2.92	222

[a] λ_{max}^{abs}: absorption maximum, λ_{max}^{em}: emission maximum at 298 K. [b] Solution state analysis using acetonitrile as a solvent. [c] Thin film state analysis was done for the thin films deposited on ITO substrate by spin coating their solution at room temperature; $\Delta\lambda^{Sol}$: Stokes shift in the acetonitrile solution; $\Delta\lambda^{film}$: Stokes shift in the thin-film state; E_g^{soln}: optical gap (in acetonitrile) at 298 K (midpoint between absorption and emission maxima); E_g^{film}: optical gap in film state (from Tauc plot); E_g^{REELS}: band gap obtained from REELS analysis; E_{HOMO} (eV) = 21.22 − E_{cutoff} + E_{onset} (from UPS spectra); E_{LUMO} (eV) = E_{HOMO} + E_g^{REELS}; T_d: thermal decomposition temperature (5% mass loss) measured by TGA.

band gap of the molecules in the solution state, estimated as the midpoint between the absorbance and emission maxima in acetonitrile[38] was determined to be 2.71 eV and 2.85 eV for **V1** and **V2**, respectively (Fig. S2†). Whereas in the film state, from the Tauc plot (Fig. 1(D)), the same is found to be 2.55 eV and 2.66 eV for **V1** and **V2** respectively.

To determine the electronic band structure of these new molecules, we conducted ultraviolet photoelectron spectroscopy (UPS) and reflection electron energy loss spectroscopy (REELS) analyses. The UPS spectra are used to locate the Fermi level (by taking the difference between the higher binding energy cutoff and He I photon energy, *i.e.*, 21.22 eV). This value is referred to as work function (Φ). Also, the HOMO energy level is obtained by adding E_{onset} (*i.e.*, lower binding energy cutoff) to the work function.[39,40] In the case of REELS analysis, we compare the inelastically scattered electrons and elastically scattered electrons (where $\Delta E = O$). This comparison helps us to obtain the electronic band structure of the molecule.[41,42] The resulting UPS and REELS spectra for both compounds are shown in Fig. 2(A) and (B) and S3† respectively. Results of these studies are summarized in Table S2.† The energy of the HOMO and LUMO levels are calculated by using eqn (1) and (2) as follows,

$$E_{HOMO}\,(eV) = 21.22 - E_{cutoff} + E_{onset} \quad (1)$$

$$E_{LUMO}\,(eV) = E_{HOMO} + E_g^{REELS} \quad (2)$$

Accordingly, the E_{HOMO} of **V1** and **V2** are found to be −5.14 eV and −5.44 eV, respectively, whereas the corresponding E_{LUMO} values are −2.65 eV and −2.92 eV. The lower HOMO and LUMO energy levels of **V2** may be due to the presence of strictly localized electron density over the 3,6-dimethoxy carbazole end groups in **V2**. But in the case of **V1**, the HOMO electron density is highly delocalized over the 4,4′-dimethoxy triphenylamine end group and the thiophene moiety (as evidenced in the DFT studies). Finally, we can construct the energy level diagram for the organic materials used in the PVSCs as shown in Fig. 2(C). The HOMO energy level of **V1** is higher than the valence band (VB) edge (−5.43 eV) of the $MAPbI_3$ perovskite material, thus providing a driving force for hole transfer from $MAPbI_3$ to **V1**. Whereas the HOMO energy level of **V2** is slightly lower than the VB of perovskite, which might be a barrier to the effective hole transfer (Fig. 2(C)). These findings imply that **V1** may be more effective for the hole extraction from $MAPbI_3$. Nonetheless, the HOMO levels of both materials are sufficiently close to the VB of $MAPbI_3$ for the effective hole transfer. Additionally, the HOMO levels of both **V1** and **V2** are lower than the work function of the counter electrode (Au), indicating that there should be no barrier to hole extraction at the cathode in the PVSCs. The LUMO energy levels of both compounds are considerably higher than the conduction band (CB) edge (−3.93 eV) of $MAPbI_3$, so both compounds can efficiently block electrons and prevent recombination with holes in the HTL layer when they are employed as HTMs in PVSCs.

To understand the thermal stability of the compounds, thermogravimetric analysis (TGA) was carried out and the resulting graph is shown in Fig. 2(D). There is no discernible decomposition in the temperature range up to 110 °C. Subsequently, a 5% decomposition of **V1** occurred at 257 °C, and **V2** showed similar behavior at 222 °C. The major decomposition of **V1** and **V2** occurs in the ranges 400–460 °C and 410–445 °C, respectively. Hence, both HTMs possess good thermal stability up to 200 °C and they are expected to be stable during device fabrication within this temperature range.

3.3. DFT studies

DFT studies of the molecules (**V1** and **V2**) were carried out to understand their structural, electronic, and charge transport properties. From these analyses, the optimized structures of **V1** and **V2** are shown in Fig. S4.† Fig. S5† represents the electrostatic potential surface mapping of **V1** and **V2**. The theoretical ring angles (dihedral angles) between the fluorene and thiophene rings in **V1** and **V2** were found to be 29.6° and 32°, respectively. Similarly, the ring angles between the thiophene and phenyl groups are 32° and 29.3°, respectively. The ring angle between the phenyl and diphenylamine groups in **V1** is 69.2°. While the ring angle between the phenyl and carbazole groups in **V2** is 54.7°. In the case of **V1**, the methoxy-substituted phenyl groups of the triphenylamine (4,4′MeO-TPA) moiety are not in the same plane, yet the tilting of these rings does not significantly impact the π-electron reorganization within the molecule, which is due to the inversion property of the sp^3 hybridized N-atom. In contrast, the carbazole moiety in **V2** experiences a different phenomenon, as the sp^2 hybridized N-atom cannot undergo such inversion as its free electrons are

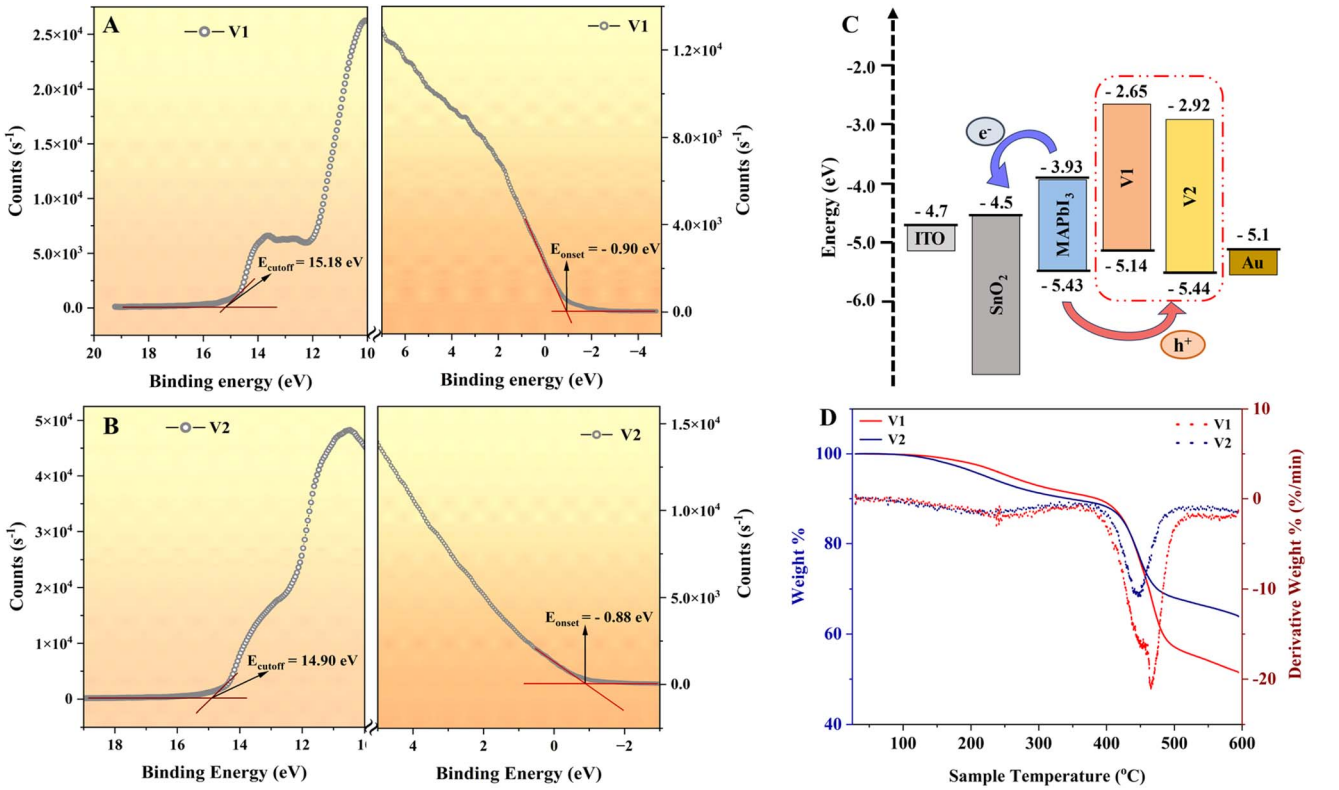

Fig. 2 UPS spectra of (A) compound **V1** and (B) compound **V2**. (C) Energy level diagram for the materials in n–i–p structured PVSCs, (D) TGA graph (solid line) and DTA graph (dotted line) for the compounds **V1** and **V2**.

involved in the aromatization. Consequently, the higher ring angle in **V1**, compared to **V2**, does not affect its electronic properties, as evidenced in the absorption studies, where the λ_{max} of **V1** was observed to be higher than that of **V2**. Moreover, due to this reason, the effective transfer of electrons from the methoxy-substituted carbazole moiety towards the central fluorene ring may get regulated; hence, these findings support the observed energy level data obtained from UPS and REELS analyses (*i.e.*, the HOMO energy level of **V2** is more negative than that of **V1**).

When it comes to the localization of the HOMO electronic cloud within the molecule, the electron density is concentrated on the triphenylamine group in **V1**, whereas it is on the carbazole moiety in **V2**. Regarding the LUMO energy state, the electron cloud is localized on the fluorene moiety of both molecules. The sequential arrangement of HOMO−1, HOMO, LUMO, and LUMO+1 energy states, as shown in the bottom-up model (Fig. 3), supports the proper ICT from the donor to the central fluorene ring in the molecules (**V1** and **V2**). The electrostatic potential surface (Fig. S5†) study indicates that the electron density is concentrated on the donor part of both molecules. Hence, the methoxy-substituted peripheral group of the HTMs is responsible for their binding affinity to the perovskite surface for improved charge transfer at the interface.

3.4. Optical studies of perovskite/HTM interface

UV-vis-NIR studies have been carried out to study the interaction between the perovskite and new HTMs, and the corresponding spectra are shown in Fig. S6.† After coating new HTMs, the perovskite's ($MAPbI_3$) absorption property does not change significantly, which ensures that the perovskite's absorption capability does not change in the presence of these HTMs. Fig. 4(A) shows the steady-state PL spectra of the perovskite thin films deposited as Glass/$MAPbI_3$/HTM and a single emission peak is observed at 763 nm. There is no significant shift in the emission maximum of the perovskite material in the presence of these HTMs. However, it is evident that the inclusion of the new HTM layers results in nearly 50% quenching of the PL intensity of $MAPbI_3$. It signifies effective interaction between the perovskite and the new HTM layer (**V1** and **V2**), which could assist in efficient hole transfer to the HTM layer in PVSCs. Thus, the steady-state PL provides qualitative information on interfacial interaction between perovskite and HTMs. To understand the charge recombination dynamics between the perovskite and HTMs, a time-resolved PL experiment was carried out and the corresponding decay curve was fitted according to a bi-exponential function given by,

$$y = y_o + A_1 e^{-(t/\tau_1)} + A_2 e^{-(t/\tau_2)} \quad (3)$$

Here, A_1 and A_2 are the relative decay amplitudes of the time components, and τ_1 and τ_2 are the lifetimes associated with the fast and slow recombination respectively.[43] The time τ_1 is associated with exciton quenching at the surface of the perovskite (due to surface defects) or at the perovskite/HTM interface, which explains the efficient charge transfer to the HTM layer.

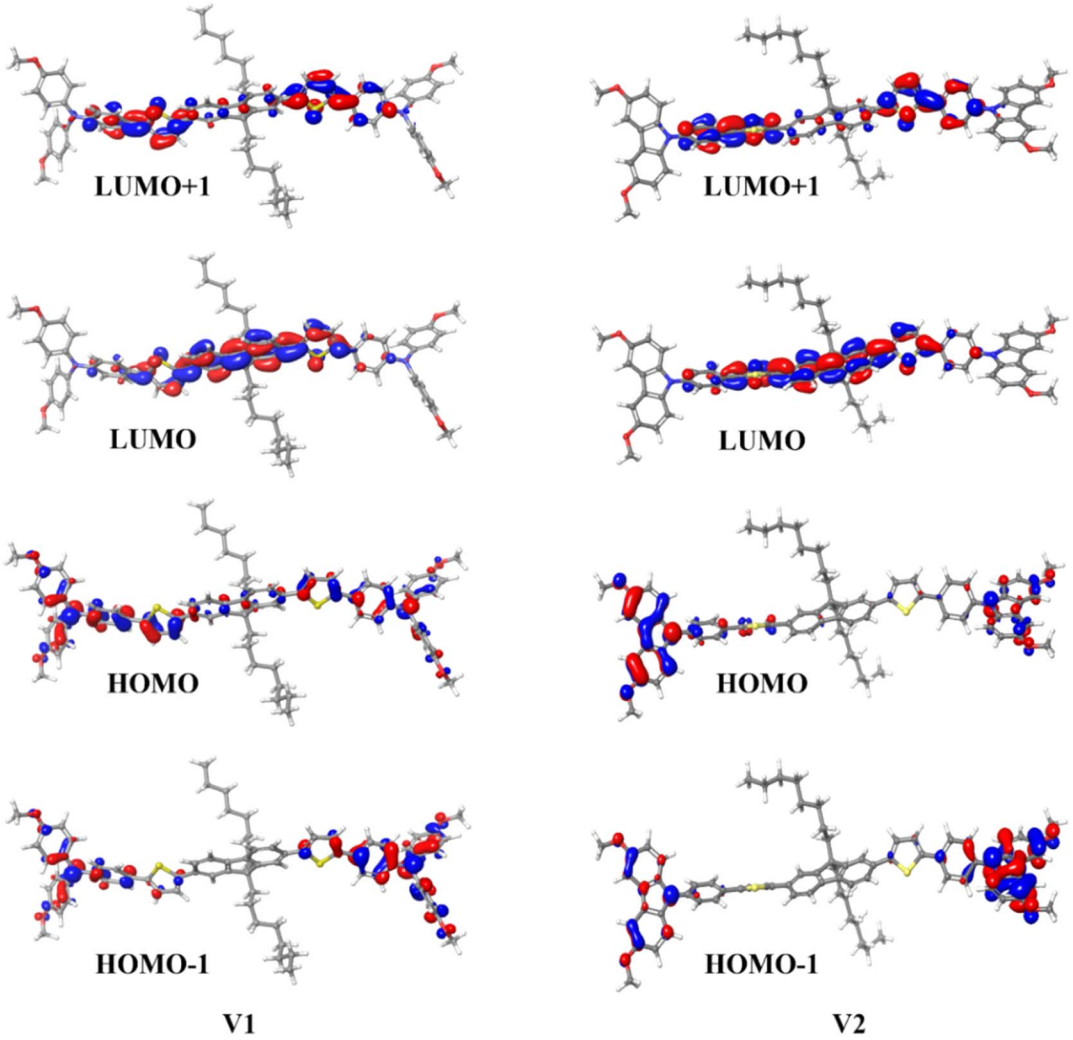

Fig. 3 Optimized molecular structures with four frontier molecular orbitals and the respective electronic distribution for compounds **V1** and **V2**.

However, the time τ_2 represents the radiative recombination of excitons in the bulk of the perovskite due to internal defects.[44,45] Fig. 4(B) shows the fitted PL decay profile for HTMs (**V1** and **V2**). The fitted data shows that the fast time component τ_1 for the devices with new HTMs decreased to about half the value for the pristine $MAPbI_3$, signifying a rapid extraction of holes from $MAPbI_3$ to the HTMs (**V1** and **V2**). The slow time component τ_2 for the perovskite film with **V1** or **V2** is 21.14 ns and 37.93 ns respectively. In other words, **V1** has better hole extraction ability than **V2** due to reduced bulk recombination of excitons in the perovskite layer. It is also validated in the study-state PL that, **V1** has a slightly superior PL quenching ability than **V2**.

Transient photo-voltaic studies (TPC/TPV) have been carried out at variable sun intensity mode to study carrier extraction and recombination dynamics. Generally, TPV is carried out at open-circuit conditions (*i.e.*, load resistance $R_L > 10^8\ \Omega$) so that after the switch-off of the laser burst, the photo-voltage undergoes fast decay. Similarly, TPC is carried out at shunted conditions (*i.e.* load resistance $R_L \sim 0\ \Omega$) so that, after the switch-off of the laser burst, the photo-generated carriers readily undergo a recombination decay. The same trends have been observed for the devices with new HTMs as shown in Fig. 4(C). In the case of the TPC study after decay fitting, a device with **V2** showed decay with a slightly higher decay timeline (*i.e.* $\tau_{\mathbf{V2}}$: 1.56 μs) than the **V1** (*i.e.* $\tau_{\mathbf{V1}}$: 0.83 μs). It suggests that excellent hole extraction is possible in a device with **V1** as HTM compared to one with **V2**. Likewise, the TPV result is shown in Fig. 4(D) illustrating the carrier recombination lifetimes (τ_{rec}). Here, we have observed that τ_{rec} for the device with **V1** is slightly longer than that of the device with **V2**. Hence, the non-radiative recombination is somewhat lower in the device with **V1** as compared to **V2**, which translates to higher V_{oc} and FF, ultimately resulting in better overall performance of the **V1**-based device.[46]

3.5. Photovoltaic and stability studies of $MAPbI_3$ solar cells

Based on the above results, the photovoltaic performance of PSCs was further investigated. We have fabricated n–i–p type (regular) PVSCs to evaluate the photovoltaic performance of the newly synthesized HTMs **V1** and **V2** (in the undoped state) with

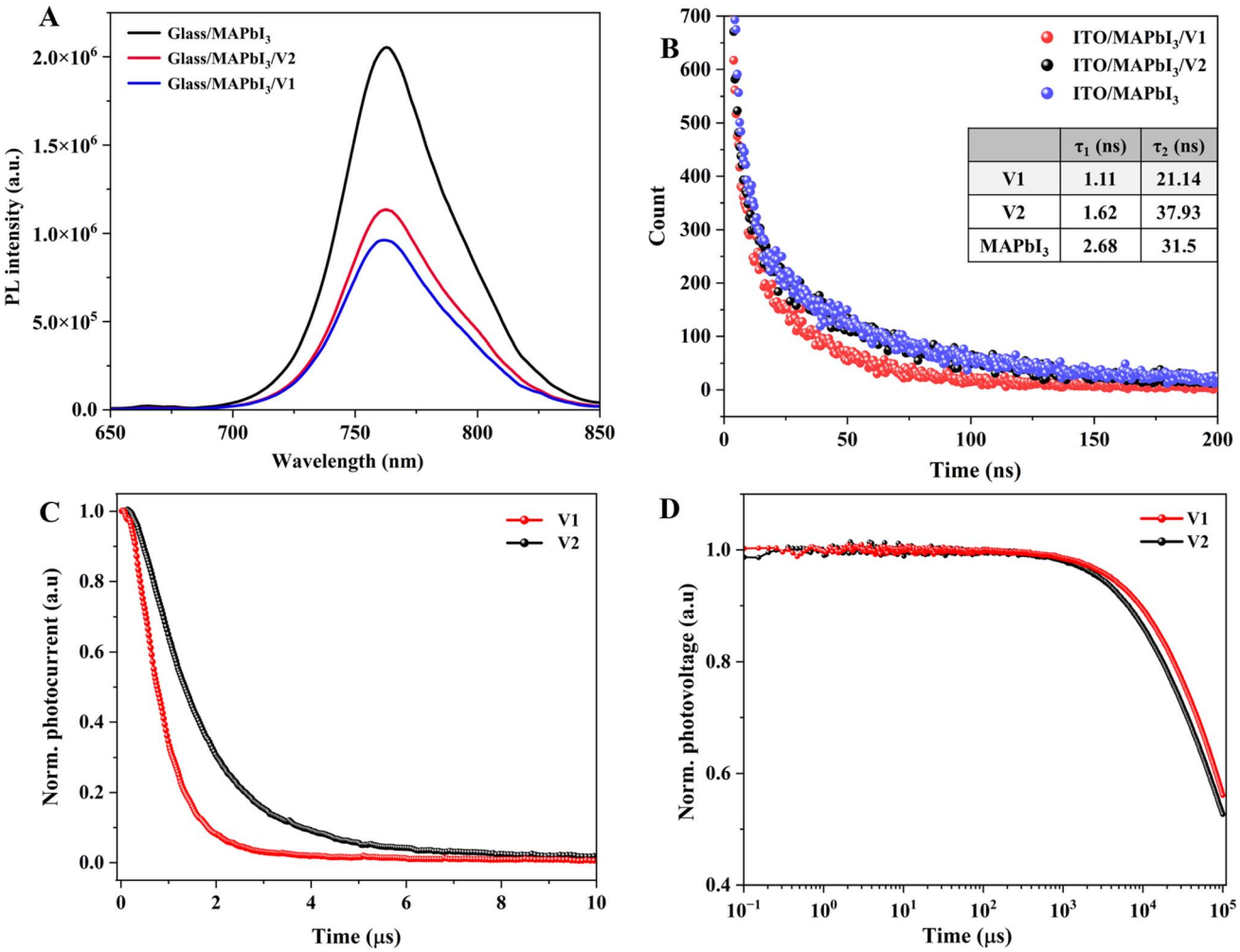

	τ_1 (ns)	τ_2 (ns)
V1	1.11	21.14
V2	1.62	37.93
$MAPbI_3$	2.68	31.5

Fig. 4 (A) Steady-state PL spectra and (B) TR-PL profiles of the perovskite thin films deposited as glass/$MAPbI_3$/HTM layers; (C) TPC and (D) TPV spectra for the PVSC with **V1** with **V2** as HTM.

device configuration ITO/SnO_2/$MAPbI_3$/HTL/Au and the schematic device structure is shown in Fig. 5(A). The device architecture is verified with the cross-sectional FE-SEM images of the fabricated PVSCs (Fig. S7(A) and (B)†). Further, Fig. S7(C) and (D)† shows the surface FE-SEM images of the developed $MAPbI_3$ on the SnO_2 layer, and Fig. S7(E)† shows the X-RD spectrum. The prominent diffraction peaks are at 14°, 24.25°, 28.54°, and 31.67°, corresponding to the (110), (022), (220), and (310) crystal planes of the $MAPbI_3$ perovskite structure, respectively.[47] PVSCs were simulated under the standard AM 1.5G, 100 mW cm^{-2} radiation, and the corresponding *J–V* curves for these cells under reverse and forward biased conditions are shown in Fig. 5(B) and S8(A) respectively.† The photovoltaic parameters of the devices are summarized in Tables 2 and S3.†

In the dopant-free and reverse-biased state, PVSC devices with new HTMs **V1** and **V2** resulted in maximum PCE of 14.05% and 12.73% respectively. In contrast, when operated in the forward bias state, the PVSCs with **V1** and **V2** attained maximum PCEs of 11.26% and 9.98%, respectively. For comparison, a PVSC without any HTM resulted in a PCE of only 2.45% (Fig. S8(B)†). Additionally, the PVSC using commercial Spiro-OMeTAD as a reference HTM (with Li-FTSI and 4-*t*BP as dopants) showed a PCE of 20.1% (Fig. S8(C)†). Here, devices with these HTMs have produced an open-circuit voltage (V_{oc}) of 1.05 V for **V1** and 1.04 V for **V2**. On looking into short-circuit current (J_{sc}) values, the device with **V1** can generate a slightly higher J_{sc} of 21.19 mA cm^{-2} as compared to the device utilizing **V2** (*i.e.*, 19.53 mA cm^{-2}). The higher J_{sc} value of **V1** is due to the strong ICT behavior and molecular stacking over **V2**, as evidenced by the optical studies. Similarly, the device with **V1** has shown a higher fill factor (FF) of 63.2%, while the device with **V2** exhibited a FF of 62.0%. Here, the higher J_{sc} and FF values for the PVSCs with **V1** are due to their relatively good hole-extracting ability as evidenced in the steady-state PL and time-resolved PL analysis. Hence, the 4,4′-methoxy triphenylamine peripheral group present in **V1** delivered superior performance in terms of V_{oc}, J_{sc} and FF compared to the one containing peripheral *N*-phenyl-3,6-methoxy carbazole moiety (*i.e.* **V2**), due to the superior ICT behavior, better molecular planarity and gradient HOMO energy level alignment. Consequently, the device using **V1** achieves a higher PCE (14.05%) than the device with **V2**.

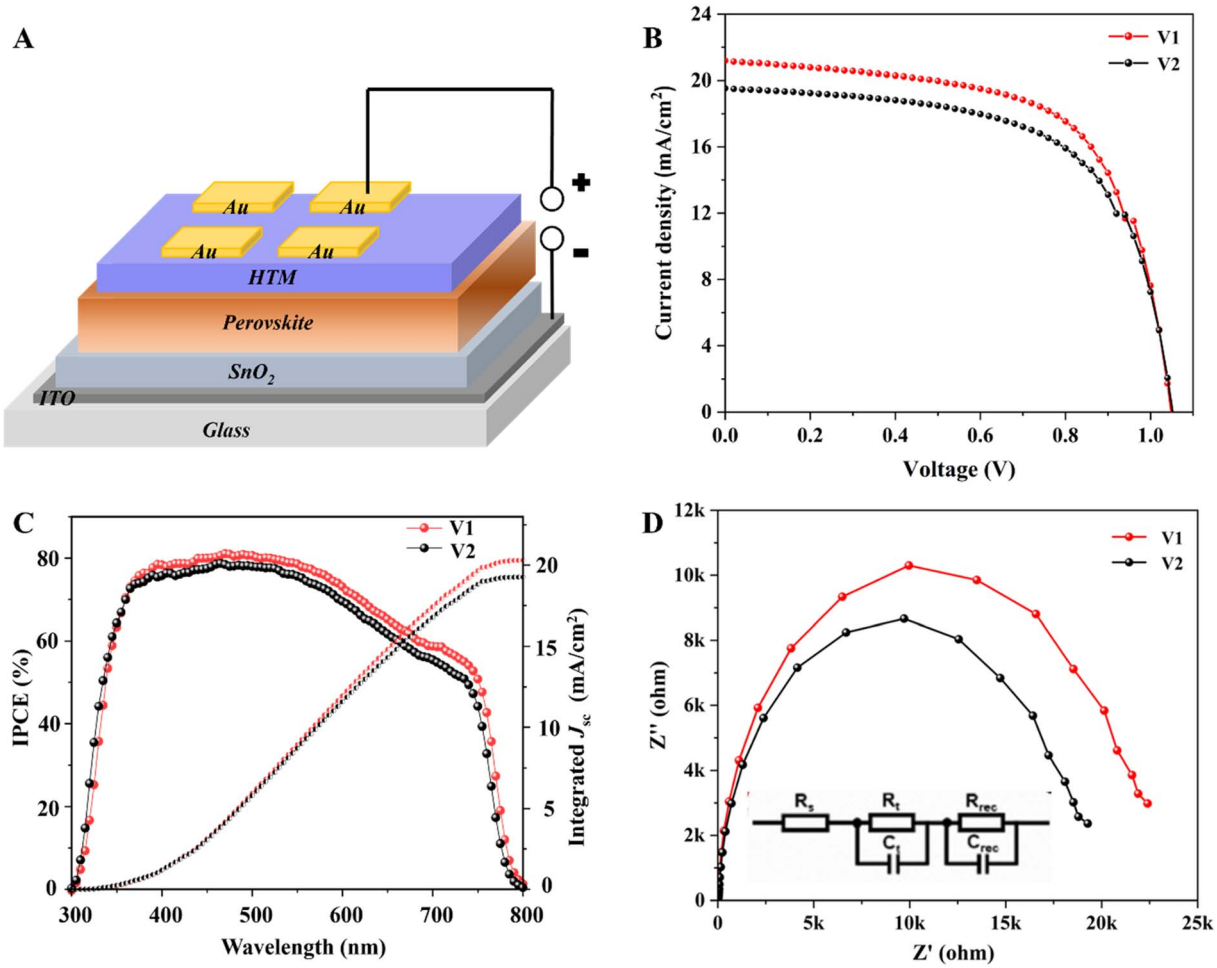

Fig. 5 (A) Architecture of fabricated device; (B) *J*–*V* characteristic curve for the PVSCs for **V1** and **V2** under reverse biased condition; (C) IPCE spectra of **V1** and **V2** based fabricated perovskite solar cells; (D) EIS analysis for the PVSCs with **V1** and **V2**.

Table 2 The *J*–*V* characteristic parameters of the PVSCs with **V1** and **V2** as HTMs (reverse biasing)

HTM	J_{sc} (mA cm^{-2})	V_{oc} (V)	FF (%)	Best PCE (%)	Avg. PCE ± S.D. (%)
V1	21.19	1.05	63.2	14.05	13.64 ± 0.2
V2	19.53	1.04	62.0	12.73	12.2 ± 0.25

The external quantum efficiency (EQE) or incident photon-to-current conversion efficiency (IPCE) spectra of devices incorporating the new HTMs **V1** and **V2** are shown in Fig. 5(C). This figure shows that the photocurrent responses across the 300–800 nm range closely match the integrated current density values, confirming that the solar simulator output aligns well with the AM 1.5G standard. Under illumination, the **V1**-based device exhibits slightly higher IPCE than the **V2**-based one, indicating more efficient photon-to-current conversion. This improvement is likely due to enhanced light harvesting and reduced charge recombination, making **V1** the more effective HTM in this context. To assess the reproducibility of device performance, a statistical distribution of the photovoltaic parameters (PCE, V_{oc}, J_{sc} and FF) for both **V1** and **V2** is depicted in Fig. S9.† We observed a much narrower distribution of all 4 parameters (V_{oc}, J_{sc}, PCE, FF) in the case of **V1** containing PVSCs over one with **V2** as HTM, which elucidates the superior reproducibility of **V1**-based PVSCs.

To investigate the internal electrical properties, we conducted an electrochemical impedance spectroscopic (EIS) analysis, and the corresponding EIS graph and Nyquist plot are shown in Fig. 5(D). To fit the EIS data, an $R_s - R_t||C_t - R_{rec}||C_{rec}$ equivalent circuit is used, where the R_s is series resistance, the R_t is charge transfer resistance, and the R_{rec} is interfacial charge recombination resistance. The arc observed at an intermediate frequency region is considered as R_{rec}. Here, the R_{rec} for a device with **V1** (R_{rec}: 22.40 kΩ) is higher than one with **V2** (R_{rec}: 19.25 kΩ), which indicates the higher carrier recombination resistance in the perovskite/**V1** interface than in the perovskite/**V2** interface and hence, confirms the higher J_{sc} value of **V1** over **V2** in the photovoltaic studies.[48]

To explore the long-term stability of these fabricated devices, we have carried out stability studies without encapsulation at room temperatures and the results are represented in Fig. 6(A). The device with **V1** has shown 75% retention of its initial PCE

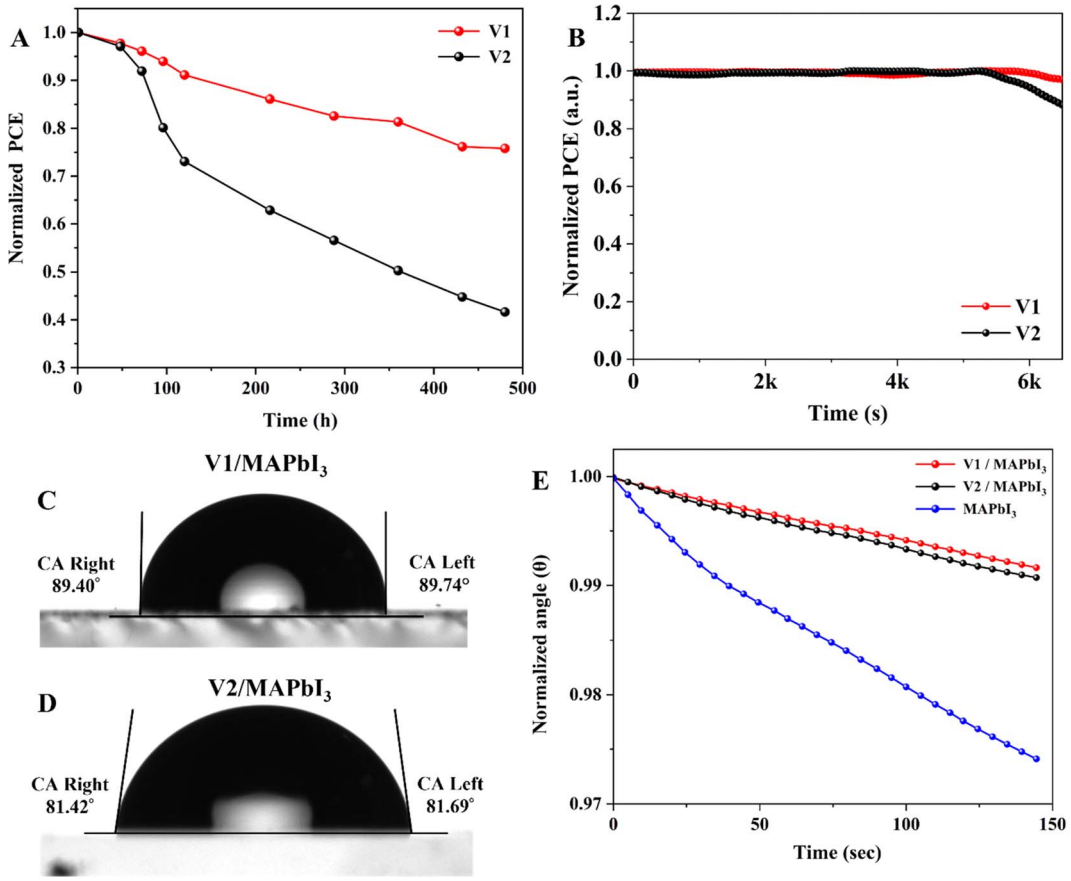

Fig. 6 (A) Stability analysis of fabricated PVSCs with **V1** and **V2** without encapsulation at room temperatures; (B) maximum power point (MPP) tracking stability test of **V1** and **V2** based unencapsulated PVSCs; contact angle measurements for (C) **V1**/$MAPbI_3$ surface, (D) **V2**/$MAPbI_3$ surface, (E) graph of the time-dependent contact angle study of the pristine $MAPbI_3$, **V1**/$MAPbI_3$ surface and **V2**/$MAPbI_3$ surface.

up to 480 hours, whereas the device with **V2** has retained 75% of the initial PCE for 113 hours. Hence, PVSCs with **V1** as HTM possess long-term stability compared to **V2**-based devices. The real-time performance of the fabricated PVSCs is evaluated under continuous illumination at standard one sun intensity (AM 1.5 G, 100 mW cm^{-2}) through maximum power point tracking (MPPT). The results of this analysis are presented in Fig. 6(B) and Fig. S10.† Under MPPT conditions, devices with **V1** and **V2** as HTM could maintain most of their initial performance for up to 5500 seconds. Meanwhile, the PVSCs with **V1** demonstrated notably better performance retention compared to those with **V2**.

To understand the effect of the hydrophobic nature of HTMs on device stability, we have measured the water contact angle (CA) for the HTM layer deposited on the perovskite layer. Table S4† provides detailed information on the contact angle analysis of materials and their interfaces. The pristine $MAPbI_3$ showed an average contact angle of 60.08°. The contact angles for pristine **V1** and **V2** are found to be 98.62° and 98.32°, respectively (Fig. S11†). Whereas, the contact angles for **V1** and **V2** on the $MAPbI_3$ surface are found to be 89.57° and 81.56° respectively, as shown in Fig. 6(C and D). This indicates only a slight decrease in CA for the new HTM/perovskite surfaces. The time-dependent change in contact angle study effectively revealed the perovskite-protecting ability of the HTMs (Fig. 6(E)). The contact angle for pristine $MAPbI_3$ decreased significantly, while both HTM/$MAPbI_3$ surfaces displayed a much slower decrease (*i.e.*, less than 0.01° per 2.5 min). Notably, the **V1**/$MAPbI_3$ surface showed superior hydrophobicity, which supports the higher stability of **V1**-based PVSCs observed in stability studies. The higher contact angle for **V1** and **V2** can be attributed to the alkyl chains on the C9 carbon of the fluorene moiety. Generally, such alkyl chains improve the hydrophobic character of an organic molecule. Consequently, the superior hydrophobicity of the undoped HTMs **V1** and **V2** could assist in improving the lifetime of PVSCs.[49]

4. Conclusions

In summary, we investigated the photovoltaic performance of two newly designed, dopant-free HTMs, **V1** and **V2**, in regular $MAPbI_3$ PVSCs. Both HTMs possess a D–π–D molecular architecture, with alkylated fluorene as a core. **V1** exhibited superior absorption and emission properties compared to **V2**, indicating superior ICT behavior in **V1**, which is further supported by DFT calculations. Both compounds (**V1** and **V2**) showed suitable HOMO and LUMO energy levels for effective hole extraction in conjunction with $MAPbI_3$ and the gold electrode. The TGA

analysis of **V1** and **V2** revealed a minimal weight loss (5%) up to 200 °C, confirming their thermal stability. TRPL and transient absorption studies demonstrated more efficient hole extraction for **V1** and reduced non-radiative recombination at the **V1**/perovskite interface. The PVSC devices with undoped **V1** and **V2** showed maximum PCE of 14.05% and 12.73%, respectively, and both materials can protect the perovskite layer from moisture due to their hydrophobicity. The PVSC containing **V1** as HTM has good reproducibility and is capable of retaining 75% of its initial PCE for 480 hours in an unencapsulated state at room temperature and relative humidity of 60%. Also, MPPT studies showed that **V1** outperformed **V2** in photophysical stability over 90 minutes. EIS measurements revealed higher charge recombination resistance for the devices employing **V1** as HTM than those with **V2**. In conclusion, our studies highlight a promising approach of integrating essential molecular properties of a HTM through facile molecular design, and the donor moiety 4,4′-methoxy triphenylamine (**V1**) is more effective than the *N*-phenyl-3,6-methoxy carbazole (**V2**) group for the photovoltaic performance and longevity of PVSCs.

Data availability

The data supporting this article have been included as part of the ESI.†

Conflicts of interest

The authors declare no conflicts of interest.

Acknowledgements

VGB acknowledges the financial support from DST, India, through the DST-INSPIRE Fellowship program (INSPIRE Fellow code: IF190931). SKS and UKD are thankful to DST, India for funding through the India-ASEAN collaborative research project (Grant No. CRD/2020/000260). AS acknowledges NITK, Surathkal for the research fellowship. The authors are thankful to CRF, NITK Surathkal for providing the instrumental facilities. KSK acknowledges the support from the EMS Sustainability Fund. BP acknowledges the financial support provided by the Materials Research Institute and their facilities at MCL. KSK and IMA acknowledge support from Doumon's SEMDE research group.

References

1 P. Mahajan, B. Padha, S. Verma, V. Gupta, R. Datt, W. C. Tsoi, S. Satapathi and S. Arya, *J. Energy Chem.*, 2022, **68**, 330–386.
2 L. Calió, S. Kazim, M. Grätzel and S. Ahmad, *Angew. Chem., Int. Ed.*, 2016, **55**, 14522–14545.
3 G. Kim, H. Choi, M. Kim, J. Lee, S. Y. Son and T. Park, *Adv. Energy Mater.*, 2020, **10**, 1–30.
4 Z. Shariatinia, *Renewable Sustainable Energy Rev.*, 2020, **119**, 109608.
5 X. P. Xu, S. Y. Li, Y. Li and Q. Peng, *Rare Met.*, 2021, **40**, 1669–1690.
6 T. Swetha and S. P. Singh, *J. Mater. Chem. A*, 2015, **3**, 18329–18344.
7 A. Krishna and A. C. Grimsdale, *J. Mater. Chem. A*, 2017, **5**, 16446–16466.
8 L. Nakka, Y. Cheng, A. G. Aberle and F. Lin, *Adv. Energy Sustainability Res.*, 2022, **3**(8), 2200045.
9 Z. H. Bakr, Q. Wali, A. Fakharuddin, L. Schmidt-Mende, T. M. Brown and R. Jose, *Nano Energy*, 2017, **34**, 271–305.
10 E. Kasparavicius, A. Magomedov, T. Malinauskas and V. Getautis, *Chem.–Eur. J.*, 2018, **24**, 9910–9918.
11 A. Magomedov, E. Kasparavičius, K. Rakstys, S. Paek, N. Gasilova, K. Genevičius, G. Juška, T. Malinauskas, M. K. Nazeeruddin and V. Getautis, *J. Mater. Chem. C*, 2018, **6**, 8874–8878.
12 E. Kasparavicius, M. Franckevičius, V. Malinauskiene, K. Genevičius, V. Getautis and T. Malinauskas, *ACS Appl. Energy Mater.*, 2021, **4**, 13696–13705.
13 D. Wang, M. Wright, N. K. Elumalai and A. Uddin, *Sol. Energy Mater. Sol. Cells*, 2016, **147**, 255–275.
14 D. Bharath, M. Sasikumar, N. R. Chereddy, J. R. Vaidya and S. Pola, *Sol. Energy*, 2018, **174**, 130–138.
15 K. Manda, V. D. Jadhav, P. Chetti, R. Gundla and S. Pola, *Org. Electron.*, 2025, **136**, 107153.
16 G. Maddala, R. Gade, J. Ahemed, S. Kalvapalli, N. B. Simhachalam, P. Chetti, S. Pola and R. Mitty, *Sol. Energy*, 2021, **226**, 501–512.
17 H. D. Pham, L. Gil-Escrig, K. Feron, S. Manzhos, S. Albrecht, H. J. Bolink and P. Sonar, *J. Mater. Chem. A*, 2019, **7**, 12507–12517.
18 A. Jegorovė, J. Xia, M. Steponaitis, M. Daskeviciene, V. Jankauskas, A. Gruodis, E. Kamarauskas, T. Malinauskas, K. Rakstys, K. A. Alamry, V. Getautis and M. K. Nazeeruddin, *Chem. Mater.*, 2023, **35**, 5914–5923.
19 C. Hao, X. Zong, Y. Cheng, M. Zhao, M. Luo, Y. Zhang and S. Xue, *Sustainable Energy Fuels*, 2021, **5**, 5548–5556.
20 W. Chi and S. K. Banerjee, *Small*, 2020, **16**, 1907531.
21 T. Niu, W. Zhu, Y. Zhang, Q. Xue, X. Jiao, Z. Wang, Y.-M. Xie, P. Li, R. Chen, F. Huang, Y. Li, H.-L. Yip and Y. Cao, *Joule*, 2021, **5**, 249–269.
22 K. S. Keremane, I. M. Abdellah, P. Naik, A. El-Shafei and A. V. Adhikari, *Phys. Chem. Chem. Phys.*, 2020, **22**, 23169–23184.
23 Z.-Z. Sun, P.-P. Sun, S. Feng, Y.-L. Xu and J.-F. Liu, *Synth. Met.*, 2019, **254**, 34–41.
24 Y. Ou, A. Sun, H. Li, T. Wu, D. Zhang, P. Xu, R. Zhao, L. Zhu, R. Wang, B. Xu, Y. Hua and L. Ding, *Mater. Chem. Front.*, 2021, **5**, 876–884.
25 P. Agarwala and D. Kabra, *J. Mater. Chem. A*, 2017, **5**, 1348–1373.
26 K. R. Prashanth Kumar, M. G. Murali and D. Udayakumar, *Des. Monomers Polym.*, 2014, **17**, 7–18.
27 R. Fuentes Pineda, Y. Zems, J. Troughton, M. R. Niazi, D. F. Perepichka, T. Watson and N. Robertson, *Sustainable Energy Fuels*, 2020, **4**, 779–787.
28 T. A. Schaub, T. Mekelburg, P. O. Dral, M. Miehlich, F. Hampel, K. Meyer and M. Kivala, *Chem.–Eur. J.*, 2020, **26**, 3264–3269.

29 K. Radhakrishna, S. B. Manjunath, D. Devadiga, R. Chetri and A. T. Nagaraja, *ACS Appl. Energy Mater.*, 2023, **6**, 3635–3664.
30 M. SasiKumar, G. Maddala, M. Ambapuram, M. Subburu, J. R. Vaidya, S. N. Babu, P. Chetti, R. Mitty and S. Pola, *Sustainable Energy Fuels*, 2020, **4**, 4754–4767.
31 L. Lin, T. W. Jones, T. C. Yang, N. W. Duffy, J. Li, L. Zhao, B. Chi, X. Wang and G. J. Wilson, *Adv. Funct. Mater.*, 2021, **31**, 2008300.
32 H. S. Jung, G. S. Han, N.-G. Park and M. J. Ko, *Joule*, 2019, **3**, 1850–1880.
33 Y. Gao, K. Huang, C. Long, Y. Ding, J. Chang, D. Zhang, L. Etgar, M. Liu, J. Zhang and J. Yang, *ACS Energy Lett.*, 2022, **7**, 1412–1445.
34 W. Ke, G. Fang, Q. Liu, L. Xiong, P. Qin, H. Tao, J. Wang, H. Lei, B. Li, J. Wan, G. Yang and Y. Yan, *J. Am. Chem. Soc.*, 2015, **137**, 6730–6733.
35 A. Ashina, R. K. Battula, E. Ramasamy, N. Chundi, S. Sakthivel and G. Veerappan, *Appl. Surf. Sci. Adv.*, 2021, **4**, 100066.
36 A. Uddin and H. Yi, *Sol. RRL*, 2022, **6**(6), 2100983.
37 Y. Hou, J. Zhang, X. Zheng, Y. Lu, A. Pogrebnyakov, H. Wu, J. Yoon, D. Yang, L. Zheng, V. Gopalan, T. M. Brown, J. A. Piper, K. Wang and S. Priya, *ACS Energy Lett.*, 2022, **7**, 1657–1671.
38 K. Vandewal, J. Benduhn and V. C. Nikolis, *Sustainable Energy Fuels*, 2018, **2**, 538–544.
39 S. S. Kim, S. Bae and W. H. Jo, *Chem. Commun.*, 2015, **51**, 17413–17416.
40 Y. Rong, M. Jin, Z. Shen, D. Yang, H. Shen, Y. Feng, H. Li, Y. Liu, F. Li, R. Liu and C. Chen, *ACS Appl. Energy Mater.*, 2023, **6**, 12318–12325.
41 M. A. Isaacs, J. Davies-Jones, P. R. Davies, S. Guan, R. Lee, D. J. Morgan and R. Palgrave, *Mater. Chem. Front.*, 2021, **5**, 7931–7963.
42 R. E. Aderne, B. G. A. L. Borges, H. C. Ávila, F. von Kieseritzky, J. Hellberg, M. Koehler, M. Cremona, L. S. Roman, C. M. Araujo, M. L. M. Rocco and C. F. N. Marchiori, *Mater. Adv.*, 2022, **3**, 1791–1803.
43 K. S. Keremane, S. Prathapani, L. J. Haur, A. Bruno, A. Priyadarshi, A. V. Adhikari and S. G. Mhaisalkar, *ACS Appl. Energy Mater.*, 2021, **4**, 249–258.
44 J. G. Sánchez, E. Aktas, E. Martínez-Ferrero, A. L. Capodilupo, G. A. Corrente, A. Beneduci and E. Palomares, *Electrochim. Acta*, 2022, **432**, 141190.
45 L. Duan, Y. Chen, J. Jia, X. Zong, Z. Sun, Q. Wu and S. Xue, *ACS Appl. Energy Mater.*, 2020, **3**, 1672–1683.
46 I. M. Asuo, A. Mahdavi Varposhti, E. D. Gomez and N. Y. Doumon, *J. Mater. Chem. C*, 2024, **12**, 7562–7571.
47 K. S. Keremane, S. Prathapani, L. J. Haur, D. Bahulayan, A. V. Adhikari, A. Priyadarshi and S. G. Mhaisalkar, *Sol. Energy*, 2020, **199**, 761–771.
48 V. Kakekochi, D. W. Kuo, C. T. Chen, E. Wolcan, C. T. Chen and U. K. Dalimba, *Org. Electron.*, 2022, **102**, 106428.
49 Y. S. Kwon, J. Lim, H.-J. Yun, Y.-H. Kim and T. Park, *Energy Environ. Sci.*, 2014, **7**, 1454.